# Thermodynamics of the Quasi-Epitaxial Flavin Assembly around Various-Chirality Carbon Nanotubes

Roholah Sharifi,[†,‡] Milinda Samaraweera,[‡] José A. Gascón,[‡] and Fotios Papadimitrakopoulos*[,†,‡]

[†]Nanomaterials Optoelectronics Laboratory (NOEL), Polymer Program, Institute of Materials Science and [‡]Department of Chemistry, University of Connecticut, Storrs, Connecticut 06269-3136, United States

S *Supporting Information*

ABSTRACT: Establishing methods to accurately assess and model the binding strength of surfactants around a given-chirality single-walled carbon nanotube (SWNT) are crucial for selective enrichment, targeted functionalization, and spectrally sharp nanodevices. Unlike surfactant exchange, which is subject to interferences from the second surfactant, we herein introduce a thermal dissociation method based on reversible H^+/O_2 doping to determine SWNT/surfactant thermodynamic stability values with greater fidelity. Thermodynamic values were reproduced using molecular mechanics augmented by ab initio calculations in order to better assess $\pi-\pi$ interactions. This afforded detailed quantification of the flavin binding strength in terms of $\pi-\pi$ stacking (55–58%), with the remaining portion roughly split 3:1 between electrostatic plus van der Waals flavin mononucleotide (FMN) interdigitation and H-bonding interactions, respectively. Quasi-epitaxial $\pi-\pi$ alignment between the near-armchair FMN helix and the underlying nanotube lattice plays a crucial role in stabilizing these assemblies. The close resemblance of the thermal dissociation method to helix–coil and ligand-binding transitions of DNA opens up a unique insight into the molecular engineering of self-organizing surfactants around various-chirality nanotubes.
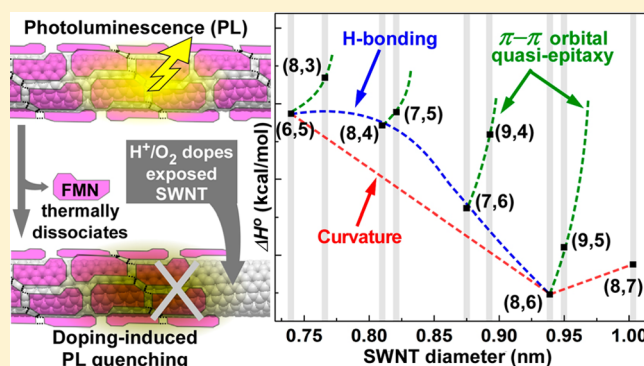
INTRODUCTION

The unique structural, optical, electronic, and thermal properties of single-walled carbon nanotubes (SWNTs) render them promising synthons for next-generation nanodevices.[1] The strong aggregation tendency of SWNTs has been a challenge for achieving stable individualized dispersions with high nanotube concentrations.[2] A variety of covalent and non-covalent functionalizations has been proposed to tackle this issue. The interruption of the extended π conjugation (responsible for the distinct optical and electronic properties of SWNTs) by covalent functionalization has directed substantial effort to optimize surfactant-based nanotube (NT) dispersions.[3] NT surfactants are amphiphatic molecules with part of their structure attracted to SWNT sidewalls and the rest promoting solubility in the dispersing medium.[3a,b] In recent years a variety of SWNT surfactants have emerged, spanning from low-molecular-weight detergents, bile salts, and pluronic[3a,b,4] and aromatic amphiphiles[5] to polymeric materials with bioactivity (e.g., DNA, polysaccharides, peptides, etc.),[6,7,5c] organic semiconductors,[8] and H-bonded assemblies.[9]

Surfactant–sidewall interactions vary in terms of both binding strength and organizational order (i.e., from random, loosely assembled to tubelike motifs).[2a,c,5a,b,6,9] Tubelike surfactant organizations, such as that of flavin mononucleotide (FMN) (Figure 1a–c) and single-stranded DNA (ssDNA), afford a highly homogeneous nanotube environment with sharp E_{ii} transitions.[6,9b] Such sharp transitions have been exploited to probe the immediate physicochemical environment of various (n,m)-chirality SWNTs.[6,9b] In 2008 our group used this concept to express the binding strength of the FMN helix to a specific (n,m)-SWNT in terms of the concentration of another surfactant [i.e., sodium dodecyl benzenesulfonate (SDBS)], which replaces FMN in a highly cooperative fashion.[9a] Nakashima and co-workers further extended this surfactant-exchange technique to link the concentration of the second surfactant (i.e., a ssDNA oligomer) with the enthalpic (ΔH) and entropic (ΔS) values governing the assembly strength of sodium cholate (SC) with various (n,m)-SWNTs.[10] Similar studies were performed by Ju and co-workers[11] on the FMN exchange with SC, SDBS, and sodium dodecyl sulfate (SDS). While these studies are highly meritorious, extracting and thoroughly understanding structure–property relationships from such surfactant-exchange thermodynamic results are challenging because of the presence of the second surfactant. This stems from the fact that the second surfactant is also likely to exhibit preferred interactions with NTs having a given diameter (d_t) and (n,m) chirality.

Because of this, our group has been searching for a technique to eliminate the need for the second surfactant. Our recent
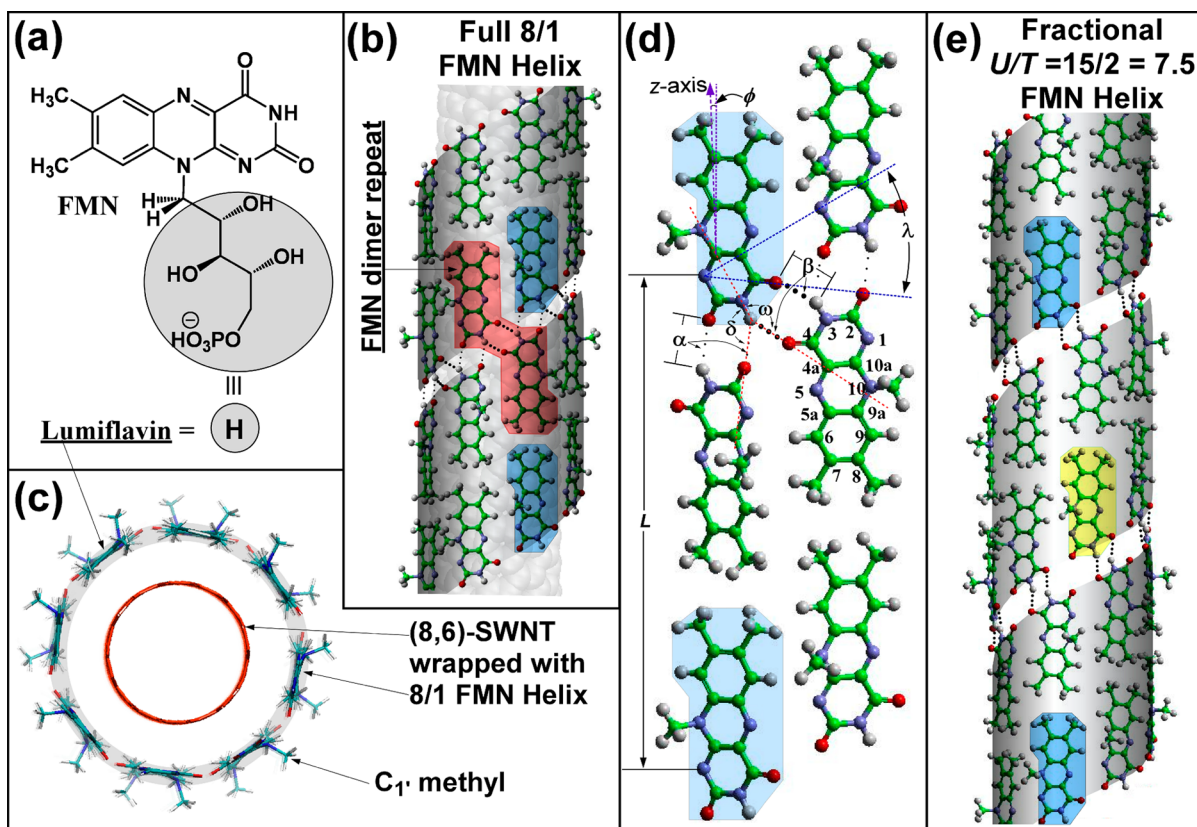
Figure 1. (a) Structures of flavin mononucleotide (FMN) and its analogue lumiflavin. (b, c) Structure of a full 8/1 FMN/lumiflavin helix wrapped around an (8,6)-SWNT. In (b), the footprint of the lumiflavin repeat is highlighted in red, and the start and end lumiflavins are highlighted in blue. (d) Spatial configuration, angular alignment, and atomic numbering of neighboring lumiflavins. (e) Fractional ($^{15}/_2$ = 7.5) FMN/lumiflavin helix, with start and end lumiflavins highlighted in blue.

study of FMN-wrapped nanotubes in H_2O or D_2O environments[12] revealed that temperature-induced dissociation of FMN can provide insights in terms of FMN binding strength on an (8,6)-SWNT that are similar if not more powerful because the technique negates the use of the second surfactant. This technique involves tracking the (n,m)-dependent E_{ii} transitions as the FMN coating dissociates and the photoluminescence of the given nanotube is quenched.

In this contribution, we show that the temperature-induced dissociation technique is a reversible process that allows us to obtain thermodynamic binding strength values [in terms of $\Delta H°$, $\Delta S°$, and $\Delta G°$ at 25 °C ($\Delta G°_{25}$)] for various FMN-wrapped semiconducting (n,m)-SWNTs. This process is based on quenching of SWNT photoluminescence (PL) upon partial FMN dissociation that exposes bare SWNT patches, which are prone to H^+/O_2-induced doping. Such partial FMN dissociation takes place at temperatures well below the point where irreversible nanotube aggregation due to substantial FMN loss occurs. With the help of molecular mechanics and ab initio molecular simulations, we have managed to delineate the underlying contributions of the helical FMN wrapping motif (full and fractional helices; Figure 1) based on (i) nanotube diameter; (ii) SWNT chiral angle; (iii) H-bonding perfection, and (iv) isotope effect. Our findings reveal that the π−π stacking interactions between FMN and SWNTs are central to the formation of these helical assemblies. Lattice commensuration plays an important role for the stability of these assemblies, and it is the strongest for near-armchair semiconducting SWNTs. Lateral interdigitation between adjacent isoalloxazine

rings constitutes the second most important factor in the stability of these assemblies, with H-bonding coming third. Three distinct H-bonding configurations have been identified as part of the various fractional helices that span between the two most stable 7/1 and 8/1 FMN helices. These findings provide for the first time a detailed understanding of the molecular motifs and relative interactions involved in the formation of such helical assemblies with quasi-epitaxial surfactant commensuration around different-chirality nanotubes. In addition, this study expands the versatility of the temperature-induced surfactant/nanotube dissociation technique and shows that under the right conditions it bears a close resemblance to heat-induced DNA[13] and protein[14] denaturation.

■ EXPERIMENTAL SECTION

Materials. HiPco SWNTs were purchased from Unidym (lot no. R0513) and used without further purification. Riboflavin 5′-monophosphate sodium salt hydrate (FMN) (73−79%) and deuterium oxide (D_2O) (99.8%) were purchased from Sigma-Aldrich and used without further purification.

Characterization. Steady-state PL spectroscopy measurements were performed on a Jobin Yvon Spex Fluorolog 3-211 spectrofluorometer equipped with a photomultiplier tube near-IR (NIR) detector. Both excitation and emission spectra were collected with a 2 nm step size, and their light intensities were corrected against instrumental variations using the Spex Fluorolog sensitivity correction factors.

Preparation of H_2O and D_2O Dispersions of FMN-Wrapped SWNTs. Aqueous dispersions of SWNTs were prepared by addition of 100 mg of HiPco SWNTs and 100 mg of FMN to 100 mL of H_2O or D_2O. The mixture was bath-sonicated for 1 h, tip-sonicated at 50%

power for 4 h (Cole Parmer Ultrasonic Processor, 300 W), and ultracentrifuged at 100000g for 10 h (Beckman, SW28 rotor) to remove the majority of nanotube bundles and large aggregates. The resulting supernatant had a clear and greenish appearance and was mostly composed of individualized FMN-wrapped SWNTs. Aliquots of 5 mL from the supernatant were mixed with 15 mL of H_2O or D_2O containing different amounts of FMN. The resultant dispersions were horn-sonicated at 40% power for 4 h (Cole Parmer Ultrasonic Processor, 300 W) at 20 °C to further improve the nanotube individualization and produce 20 mL stock FMN/SWNT dispersions with varying FMN concentrations.

Temperature-Induced Dissociation Measurements of FMN/SWNT Dispersions in H_2O and D_2O. A small amount (ca. 10 mL) of the aforementioned stock FMN/SWNTs dispersion in either H_2O or D_2O was transferred to a sample vial and incubated for 5 min in an oil bath set at the desired temperature. After the dispersion was cooled to room temperature, one-dimensional (1D) PL scans were collected at various excitation wavelengths in order to extract the PL intensities of the suspended semiconducting (n,m)-SWNTs.[9b] The resultant PL intensities were normalized to their starting PL intensities at 20 °C. The midpoint of each PL intensity versus temperature curve, herein defined as the melting temperature (T_m) of the FMN helix, was obtained by sigmoidal Boltzmann fitting.[15]

Temperature-Induced Dissociation Measurements of FMN-Wrapped (8,6)-SWNTs in an O_2-Depleted or Acidic Environment. Similar to the above, 5 mL of stock FMN/SWNTs dispersion in D_2O (pH 6.5) was either capped with a rubber septum and degassed with N_2 gas for 5 min or adjusted to pH 5.50 by dropwise addition of 0.1 M DCl solution. Subsequently, temperature-induced dissociations were conducted while at the same time both vis−NIR absorption and PL emission (739 nm excitation) spectra were obtained before the next heating interval.

Extraction of Thermodynamic Parameters from FMN/SWNT Thermal Dissociation Curves. Thermodynamic parameters in a two-state model can be obtained from the free energy changes in equilibrium measurements of a process described by eq 1:

$$\Delta G = \Delta G° + RT \ln Q \tag{1}$$

where ΔG is the free energy of the system in an arbitrary state, $\Delta G°$ is the standard-state free energy, R is the gas constant, T is the absolute temperature, and Q is the reaction quotient. At equilibrium, $\Delta G = 0$ and Q is equal to the equilibrium constant (K_{eq}), so eq 1 can be rewritten as

$$\Delta G° = -RT \ln K_{eq} \tag{2}$$

In the present case, K_{eq} is the association or affinity constant (K_A) for the binding of a ligand to a substrate: $K_{eq} = K_A = 1/K_D$, where K_D the dissociation constant. In a cooperative system with n ligands that bind with infinite cooperativity, the ligand concentration [L] equals the average dissociation constant K_D^{av}, as explained in the Supporting Information (SI). Thus, eq 2 can be modified to give

$$\Delta G° = +RT \ln[L] \tag{3}$$

Rewriting the standard-state Gibbs free energy of the aforementioned process $(\Delta G°)$ in terms of the standard-state enthalpy and entropy $(\Delta G° = \Delta H° - T\Delta S°)$ and subsequent rearrangement transforms eq 3 into the van't Hoff equation (eq 4),

$$\frac{1}{T_m} = \frac{2.3R}{\Delta H°} \log[L] + \frac{\Delta S°}{\Delta H°} \tag{4}$$

in which T_m is the melting temperature, which can be obtained from the midpoint of the sigmoidal curve as described above.

The values of T_m obtained from sigmoidal fitting for various concentrations of FMN were used to plot T_m^{-1} versus log [FMN] for each type of nanotube in both H_2O and D_2O. Linear fits provided the slopes and vertical axis intercepts, from which values of $\Delta H°$ and $\Delta S°$, respectively, and thus $\Delta G_{25}°$ for the binding of FMN onto a given (n,m)-SWNT were extracted. The estimated errors in the thermodynamic values of $\Delta H°$ and $\Delta S°$, denoted as $\sigma_{\Delta H°}$ and $\sigma_{\Delta S°}$, respectively,

were obtained using standard propagation of error formulas from the errors in the slope (σ_{slope}) and intercept $(\sigma_{intercept})$ of the T_m^{-1} versus log [FMN] linear fit, which are given in terms of the standard deviation of the fit (σ) by eqs 5 and 6, respectively:

$$\sigma_{slope} = \frac{\sigma}{\sqrt{\sum_i (x_i - \bar{x})^2}} \tag{5}$$

$$\sigma_{intercept} = \sigma \sqrt{\frac{1}{n} + \frac{\bar{x}^2}{\sum_i (x_i - \bar{x})^2}} \tag{6}$$

The estimated error in $\Delta G_{25}°$ $(\sigma_{\Delta G_{25}°})$ was calculated using eq 7:

$$\sigma_{\Delta G_{25}°} = \sqrt{(\sigma_{\Delta H°})^2 + T^2(\sigma_{\Delta S°})^2} \tag{7}$$

Verification of FMN/SWNT Dispersion Individualization. Small quantities (ca. 2 mL) of stock FMN/SWNT dispersion with a 1% w/v concentration of FMN solution in H_2O or D_2O were diluted with varying amounts of isotonic (1% w/v) FMN solution to obtain 70, 50, 33, 25, 18, 8, and 4% dilutions. The resulting dispersions were incubated at 20 °C for 1 h, and PL intensities were obtained at different excitation and emission wavelengths for all of the (n,m)-SWNTs.[9a] The resulting PL intensities were plotted as a function of decreasing nanotube concentration to ensure linearity of the fluorescence reduction for higher dilutions.

Molecular Mechanics Simulations. Molecular mechanics (MM) calculations were performed using a hybrid REBO[16]−OPLSAA[17] force field as implemented in the LAMMPS program.[18] REBO was employed to model the various (n,m)-SWNTs, while OPLSAA was used to model the FMN wrapping. FMN was represented by lumiflavin (an N-methylated isoalloxazine whose structure is shown in Figure 1a). The N_{10} lumiflavin nitrogen, where the D-ribityl chain is attached in FMN, was set in sp^3 hybridization (Figure 1d).[19] Partial charges for the lumiflavins were derived by the restrained electrostatic potential (RESP) method using density functional theory (DFT) at the B3LYP/6-31G* level.[20] Interactions of the various (n,m)-SWNTs with lumiflavin helices were modeled using a Lennard-Jones (LJ) 6−12 potential with previously reported LJ parameters for sp^2 nanotube carbons.[21] No partial charges were assigned to the nanotubes. All of the nanotubes were constructed using the TubeGen program.[22] For each (n,m)-SWNT studied, four helical FMN repeats were constructed in accordance with known methods.[9a] The long axes of the SWNT and the surrounding FMN helix were set along the z direction to ensure that their centers of mass would coincide. Energy minimizations were carried out using the conjugate gradient method.

Extraction of Perpendicular and Lateral FMN Interaction Energies. Using the energy-minimized configurations of various U/T FMN helices [where U is the number of FMN dimer repeats (Figure 1b) to complete T turns of 360°] on various (n,m)-SWNTs, we considered the following energy terms as a measure of total stability per flavin (which can be readily compared to binding enthalpies per flavin):

(i) The van der Waals (vdW) contribution of π−π stacking interactions. For a given FMN-wrapped (n,m)-SWNT, this term was derived by computing half of the LJ interaction energy between the two central lumiflavin units (shaded in red in Figure 1b) and the nanotube. Although using a simple LJ potential to describe FMN−nanotube interactions may appear too simplistic, it has been shown that LJ interactions give a good approximation of the π−π dissociation energy as two aromatic molecules separate in the direction perpendicular to their rings.[23,24] However, relative ring misalignments due to lumiflavin rotation with respect to the graphene lattice are expected to be poorly described via simple LJ interactions. To assess this effect, the orbital contribution to the π−π interaction was considered separately using DFT as presented below in the section on ab initio calculations.

(ii) The nonbonded lateral FMN−FMN interactions, composed of vdW and electrostatic contributions. These terms were computed as the interaction energy between one of the most central lumiflavins and the rest of the FMN helix. Since there are two most central

luminoflavins (shaded in red in Figure 1b), this interaction energy was averaged over these two flavins. Only for the purposes of separating and qualitatively determining the strength of H-bonds for the various FMN wraps, for a posteriori evaluation we used the Dreiding force field, which contains an explicit term for H-bonds. Parameters and the energy formula used in this term are presented in the Supporting Information.

Ab Initio Calculations To Assess the Orbital Contribution of the $\pi-\pi$ Interactions from FMN Misalignment. To study the quasi-epitaxial $\pi-\pi$ stacking energy as a function of Ω, the angle of lumiflavin rotation away from the perfectly aligned "Bernal-type" orientation, a 5×6 flat graphene subunit was constructed with 30 fused benzene rings and terminated with hydrogen atoms. A flavin was placed on the center of the 5×6 graphene subunit, after which the energy was minimized using dispersion-corrected DFT[25] and the wb97xd/6-31G(d,p) basis set, as implemented in Gaussian 09.[26] Subsequently, the lumiflavin moiety was rotated clockwise from its aforementioned optimal Bernal-type configuration in a stepwise fashion (every 2.5°), and the corresponding energy (taking into account basis set superposition error) was computed to yield the energy expenditure as a function of Ω. An additional set of energy values as a function of Ω were obtained by *xy* translation of the center of mass of the middle lumiflavin ring to a "bridged" configuration (i.e., above the middle of a graphene C–C bond)[27] and subsequent application of the Ω rotation.

RESULTS AND DISCUSSION

FMN and its derivatives present one of the highest-order surfactant organizations around SWNTs (Figure 1).[9] Such order originates from the seamless helical wrapping of an FMN ribbon stabilized via (i) cooperative H-bonding, vdW, and electrostatic interactions between adjacent isoalloxazine moieties and (ii) concentric $\pi-\pi$ stacking interactions with the underlying graphene sidewalls. Despite numerous theoretical[9a,19,28] and experimental works,[9,11,12,19] the relative contributions of these interactions remain unsettled in terms of the effect of varying diameter (d_t) and chiral angle (θ) of the tubular SWNT lattice on the stability of the FMN organization. Binding strength studies based on surfactant-exchange methods provide a valuable starting point.[9a,10,12,19] However, the variety of secondary interactions that the second surfactant and its micellar organization bring to the FMN exchange process introduces substantial perturbation in extracting "structure–property relationships" based on H-bonding, vdW, $\pi-\pi$ stacking, d_t, and θ contributions.

Our laboratory has recently shown that temperature-induced SWNT PL quenching can in principle provide FMN binding strength information similar to that of the surfactant-exchange methodology.[12] For this, highly diluted SWNT dispersions (concentrations typically lower than 5×10^{-5} $w_{SWNT}/v_{(H_2O \text{ or } D_2O)}$) were used to slow down the irreversible SWNT aggregation process. Figure 2 illustrates the temperature-induced quenching of the PL of (8,6)-SWNTs as a function of the FMN concentration in D_2O. The highly cooperative sigmoidal curves indicate the presence of an equilibrium dissociation process that shifts the transition midpoints (T_m) to higher temperatures for greater FMN concentrations. Figure S1a–c in the Supporting Information presents vis–NIR absorption spectra for low, medium, and high FMN concentrations as a function of incubation temperature. The absorbance intensity at 920 nm (residing in between the E_{22}^S and E_{11}^S spectral manifolds of FMN-wrapped SWNTs)[9b] offers an ideal point to assess the background scattering, which is proportional to the degree of SWNT aggregation. As shown at the bottom of Figure 2 (right ordinate), the 920 nm
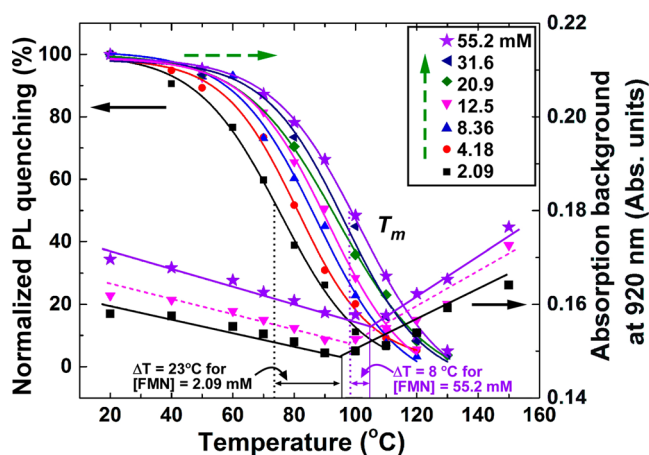

Figure 2. Normalized PL quenching of FMN-wrapped (8,6)-SWNTs in D_2O as a function of exposure temperature and FMN concentration in the surrounding medium. The excitation and emission wavelengths were 739 and 1212 nm, respectively. PL quenching at each temperature was obtained by initially incubating at the specified temperature and then cooling to room temperature (25 °C) and measuring the PL intensity (peak height at 1212 nm) before advancing to the next high temperature. The right ordinate shows the absorption background at 920 nm for three FMN concentrations.

background absorption first starts with a shallow decrease from 20 to 100 °C and then abruptly increases above 120 to 130 °C. From linear fits to the downward and upward sections, the onset temperature of nanotube aggregation can be estimated. Such an aggregation onset takes place at a temperature that is $\Delta T \approx 23$ °C higher than the temperature the midpoint of PL quenching for the lowest FMN concentration (2.09 mM) (Figure 2). At the highest FMN concentration (55.2 mM), the value of ΔT drops to 8 °C.

Since larger FMN concentrations in the surrounding medium push the T_m transition to higher temperatures, the origin of such temperature-induced PL quenching appears to be linked to FMN dissociation. Moreover, NT aggregation is not intimately involved with the PL quenching process, since it displays a higher onset temperature and different curve shape. This directed us to investigate a doping-induced quenching process, in view of the fact that these experiments were conducted in weakly acidic (pH 6.5) FMN-buffered solutions and O_2-saturated aqueous media.[29] Under these conditions, any defect in the seamless FMN helix is expected to expose the underlying graphene lattice and induce doping according to the redox reaction shown in the inset of Figure 3.[29,30] In view of the large exciton diffusion length in SWNTs (greater than 50 nm),[31] a progressive increase in the number and area of exposed SWNT patches as part of FMN dissociation would be expected to progressively lower the number of excitons that recombine radiatively and hence would explain the sigmoidal temperature-induced PL quenching curve. To test this theory, we conducted two extra experiments with FMN-wrapped SWNTs in (a) an O_2-depleted pH 6.5 D_2O medium and (b) an O_2-saturated, pH 5.5 D_2O medium. In accordance with Le Chatelier's principle, increasing the H^+ concentration would be expected to push the reaction forward (more doping), while decreasing the O_2 content should favor the backward reaction (less doping). If acid-induced doping is the cause of such SWNT PL quenching, then the acidified solution should shift the entire sigmoidal transition to lower temperatures, while the O_2-depleted solution should shift it to higher temperatures. As

shown in Figure 3, this was indeed the case, as T_m moved from 87 °C to 81 and 93 °C for the acidified and O_2-depleted
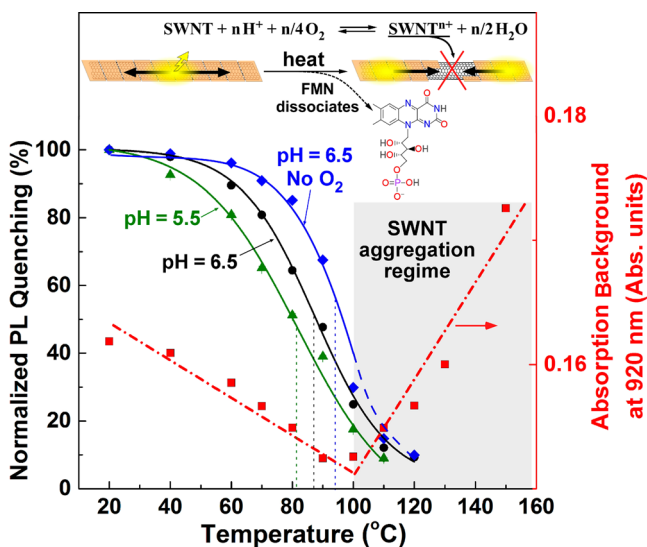
Figure 3. Normalized photoluminescence (PL) intensity (left ordinate) and optical absorption background (right ordinate) as functions of temperature for FMN-wrapped (8,6)-SWNTs dispersed in D_2O with various pH and O_2 contents. The inset at the top illustrates that the partial thermal dissociation of the FMN helix creates exposed SWNT patches, which are prone to acid doping (according to the reaction shown above). This creates nonradiative traps for the excitons that diffuse to the exposed patches, which progressively lowers the PL intensity before nanotube aggregation sets in. The excitation and emission wavelengths were 739 and 1212 nm, respectively.

solutions, respectively. Here it is important to stress that the aggregation onset temperature stayed the same (i.e., 100 °C), as determined by the 920 nm background absorption intensity (Figure S2). This provides unequivocal proof that doping is the underlying cause for the sigmoidal PL quenching, as it gets more opportunity to dope the exposed SWNT segments from the progressive FMN dissociation occurring at higher temperatures.

One last question that needs to be addressed is whether the PL emission at the sigmoidal transition originates purely from FMN-wrapped SWNT segments or also possesses contributions from the exposed SWNT portions. The strong $\pi-\pi$ stacking of FMN with SWNTs is known to cause significant red shifts (from 10 to 50 nm) in the emission maxima of all (n,m)-SWNTs.[9a] Correspondingly, if the unexposed SWNT regions are emissive, they would be expected to show a blue shift. Figure S3 illustrates the (8,6)-SWNT PL spectra as a function of incubation temperature in all three of the aforementioned environments. By tracking the emission maxima as a function of temperature, we witness no shift until 120 °C, where a red shift due to NT aggregation takes place.[32] This indicates that (i) the exposed nanotube areas are shorter than the exciton diffusion length and emission takes place solely within the FMN-wrapped SWNT segments and (ii) the PL signature for aggregation takes place ca. 20 °C higher than that estimated for optical background absorption (i.e., Figures 2, 3, and S2). These two points suggest that the majority of the sigmoidal PL quenching curve is devoid of noncooperative aggregation interferences. Moreover, as shown in Figure S4, in the SWNT concentration regime where all of the experiments were

conducted, there is a linear correlation of the PL intensity with nanotube concentration. In addition, as shown in Figure S5a, prior to the onset of the sigmoidal transition, incubation of the FMN-wrapped nanotubes at various temperatures has no effect on the PL intensity at 25 °C, which recovers to its initial value (within 3%). Similarly, the buffering ability of FMN provides a stable pH environment that changes only minutely (from pH 6.51 to 6.45) over the entire experimental range of FMN concentrations (Figure S5b).

On the basis of the aforementioned analysis, the PL quenching curves in Figure 2 [i.e., (8,6)-SWNTs in D_2O] and those of all other (n,m)-SWNTs whose luminescence was strong enough in D_2O (Figure S6) and H_2O (Figure S7) were used to extract T_m as a function of the FMN concentration in the surrounding medium. Such temperature-induced dissociation bears close resemblance to denaturation transitions of DNA[13b,a] and proteins.[14] By means of a similar theoretical treatment, the T_m values for various (n,m)-SWNTs with different FMN concentrations and dispersing media (H_2O vs D_2O) were used to extract the thermodynamic $\Delta H°$ and $\Delta S°$ values for the stability of the respective FMN helices. Data analyses are described in the Experimental Section, while the theory behind the data treatment is presented in the Supporting Information. From the slopes and intercepts of linear fits to the plots of T_m^{-1} as a function of log [FMN] (Figure 4a for H_2O and Figure S8 for D_2O), values of $\Delta H°$ and $\Delta S°$ can be extracted according to eq 4. The individual linear fits responsible for extraction of $\Delta H°$ and $\Delta S°$ values for various (n,m)-SWNTs are shown in Figures S9 and S10 for the two dispersing media. Table 1 lists the thermodynamic values and results of error analysis (as described in the Experimental Section) for all of the nanotubes studied. The ΔG values were calculated at a temperature of 25 °C ($\Delta G_{25}°$).

Solvent Isotope Effect and Chirality Dependence. It was recently shown (by both surfactant-exchange and thermal-dissociation methods) that the helical wrapping of FMN around (8,6)-SWNTs is more stable in D_2O than in H_2O as the dispersing medium.[12] This was attributed to stronger hydrophobic interactions and H-bonding in D_2O as opposed to H_2O.[33] Such a pattern is maintained for all of the FMN-wrapped (n,m)-SWNTs, as shown in Figure 4b−d. The similar (n,m) patterns in the D_2O and H_2O values for $\Delta H°$, $\Delta S°$, and $\Delta G_{25}°$ indicate that the greater stability of the FMN helices in D_2O is not a function of nanotube diameter (d_t). Upon closer inspection, there is a notable difference for nanotubes with similar d_t and different chiral angle θ (shown by the greater lengths of the solid red lines vs the solid black lines in Figure 4b−d). Table S1 in the Supporting Information lists the $\Delta H°$ differences as a function of θ for four nanotube pairs with similar d_t: (6,5) vs (8,3); (7,5) vs (8,4); (7,6) vs (9,4); and (8,6) vs (9,5). In each pair, the first nanotube is near-armchair ($\theta \approx 24−27°$), while the second has a lower chiral angle ($\theta \approx 15−20°$). The mean $\Delta H°$ differences in D_2O and H_2O are −4.7 and −2.7 kcal/mol for near-armchair and lower-θ SWNTs, respectively. This indicates that in D_2O, FMN helices on near-armchair nanotubes gain greater stability than their lower-θ counterparts, as opposed to those in H_2O. The last two columns in Table S1 define the near-armchair versus lower-θ percent differences. This difference is 2.6 times higher in D_2O as opposed to H_2O (i.e., −10.0 vs 3.8%, respectively). This difference stems from the stronger hydrophobic interactions in D_2O that bring the flavin moieties closer to the nanotube lattice.[12] Correspondingly, any quasi-epitaxial misalignment
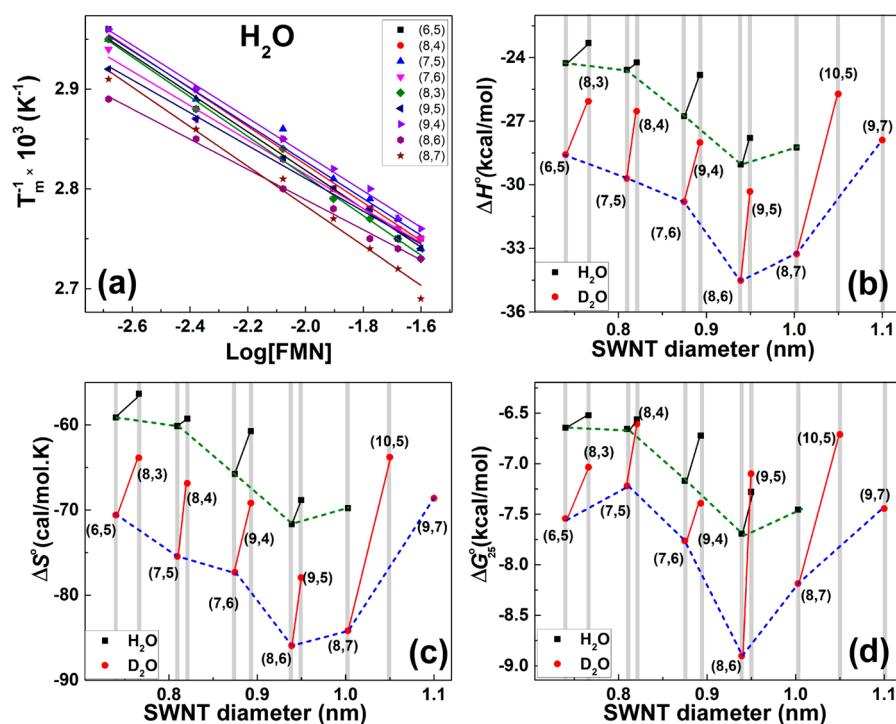
Figure 4. (a) Plots of T_m^{-1} as a function of log [FMN] for different FMN-wrapped (n,m)-SWNTs dispersed in H_2O. (b–d) Plots of $\Delta H°$, $\Delta S°$, and $\Delta G_{25}°$, respectively, as functions of SWNT diameter (d_t) for both H_2O and D_2O dispersions. All near-armchair semiconducting (n,m)-SWNTs are interpolated with dashed lines, while values for nanotubes with similar d_t are connected with solid lines. The excitation and emission wavelengths for (6,5), (8,4), (7,5), (7,6), (8,3), (9,5), (9,4), (8,6), (8,7), (10,5), and (9,7) SWNTs were 582, 608, 655, 666, 678, 689, 737, 739, 747, 805, and 812 nm and 1004, 1148, 1070, 1164, 994, 1282, 1154, 1212, 1316, 1294, and 1376 nm, respectively.

Table 1. Thermodynamic Parameters Extracted Using Temperature-Induced Dissociation of FMN-Wrapped (n,m)-SWNTs in H_2O and D_2O as Dispersing Media

(n,m)	$\Delta H°$ (kcal/mol)		$\Delta S°$ (cal/mol)		$\Delta G_{25}°$ (kcal/mol)	
	H_2O	D_2O	H_2O	D_2O	H_2O	D_2O
(6,5)	−24.3 ± 1.0	−28.6 ± 0.5	−59.1 ± 0.4	−70.6 ± 0.2	−6.6 ± 1.0	−7.5 ± 0.5
(8,3)	−23.3 ± 0.8	−26.1 ± 1.1	−56.3 ± 0.3	−63.9 ± 0.4	−6.5 ± 0.8	−7.0 ± 1.1
(7,5)	−24.6 ± 1.2	−29.7 ± 0.5	−60.1 ± 0.5	−75.4 ± 0.2	−6.7 ± 1.2	−7.2 ± 0.5
(8,4)	−24.2 ± 0.7	−26.5 ± 0.9	−59.3 ± 0.3	−66.9 ± 0.3	−6.6 ± 0.7	−6.6 ± 0.9
(7,6)	−26.8 ± 0.9	−30.8 ± 1.4	−65.8 ± 0.3	−77.3 ± 0.4	−7.2 ± 0.9	−7.8 ± 1.4
(9,4)	−24.8 ± 0.6	−28.0 ± 0.8	−60.7 ± 0.2	−69.2 ± 0.3	−6.7 ± 0.6	−7.4 ± 0.8
(8,6)	−29.0 ± 0.9	−34.5 ± 1.3	−71.6 ± 0.3	−85.9 ± 3.5	−7.7 ± 0.9	−8.9 ± 1.7
(9,5)	−27.8 ± 1.0	−30.3 ± 0.8	−68.8 ± 0.4	−77.9 ± 0.2	−7.3 ± 1.0	−7.1 ± 0.8
(8,7)	−28.2 ± 1.0	−33.3 ± 0.2	−69.8 ± 0.3	−84.2 ± 0.1	−7.4 ± 1.0	−8.2 ± 0.2
(10,5)	−	−25.7 ± 1.4	−	−63.8 ± 0.5	−	−6.7 ± 1.4
(9,7)	−	−27.9 ± 0.6	−	−68.6 ± 0.2	−	−7.4 ± 0.6

between the FMN isoalloxazine rings and (n,m)-SWNT lattice are expected to be more pronounced in D_2O as opposed to H_2O. This provides the first indication that quasi-epitaxy is possibly a key factor in stabilizing the helical FMN assembly. Such a realization can easily explain why (n,m)-SWNTs with θ < 15° are not individualized in significant abundance to allow determination of $\Delta H°$, $\Delta S°$, and $\Delta G_{25}°$.

SWNT Diameter Dependence. The blue and green dashed lines in Figure 4b–d present the d_t dependences of $\Delta H°$, $\Delta S°$, and $\Delta G_{25}°$ for near-armchair nanotubes in D_2O and H_2O, respectively. In agreement with various experimental results (based on surfactant-exchange methods),[9a,10−12] the thermal dissociation results presented herein verify that the FMN helix around (8,6)-SWNTs (d_t = 0.94 nm) possesses the highest binding strength. This affinity decreases for both smaller- and larger-diameter nanotubes. Upon closer inspection of the $\Delta G_{25}°$ results (Figure 4d), it appears that the FMN assembly around (6,5)-SWNTs creates another energy minimum. This minimum was also observed in our surfactant-exchange results,[9a] and for the reader's convenience, it is replotted in Figure S11 together with the $\Delta G_{25}°$ results of Figure 4d in D_2O (blue dashed line). In a separate work,[9b] it was mentioned that the (6,5)-SWNT is wrapped by a 7/1 FMN helix, as opposed to the 8/1 FMN helix accommodated by the (8,6)-SWNT. In between these two nanotubes, the stability trends deviate significantly from the linear increase in FMN binding strength predicted by Ogunro and Wang[28] on the basis of increasing π−π overlap of the flat isoalloxazine rings with the less curved graphene lattices of larger nanotubes. For larger than (8,6)-SWNTs, the FMN assembly steeply looses its

stability, which contradicts the theoretically predicted increase in $\pi-\pi$ overlap for larger d_t nanotubes.[28] The close similarity between the H_2O and D_2O results suggests that the steep drop in binding strength for SWNTs larger than (8,6)-SWNTs is not isotopically driven but rather originates from within the FMN assembly.

Molecular Mechanics Simulations. In order to gain a meaningful understanding in terms of the structure−property relationships that control the helical FMN organization around various (n,m)-SWNTs, we turned our attention to molecular simulations. The incommensurable nature of various FMN helices around given (n,m)-SWNTs precludes the use of periodic boundary conditions. This, in turn, prohibits the use of full-fledged ab initio calculations (because of system dimensions) with equal footage for all FMN-wrapped nanotubes. For each type of (n,m)-SWNTs studied, an FMN helix with four turns was constructed and energy-optimized using the conjugate gradient method. An exhaustive search of optimal configurations was performed to find the lowest-energy structure of the FMN helix constructed around a given (n,m)-SWNT. This was carried out by constructing a scanning grid, keeping the nanotube fixed, and rotating the isoalloxazine rings within their helices as well as displacing the helix up and down along the z axis to find an optimum configuration. Using the lowest-energy configurations of the various FMN helices on different (n,m)-SWNTs, the total interaction energies per flavin were constructed with the following two terms: (i) the vdW-based $\pi-\pi$ stacking energy contribution and (ii) the lateral FMN−FMN interactions that include both Coulombic and vdW contributions. Considerable attention was given to eliminate end effects that arise from loosely bound lumiflavins on either end of the four-turn helices by considering only the innermost lumiflavin repeat. Last but not least, the N_{10} nitrogen of lumiflavin, where the $C_{1'}$ methyl group is attached (Figure 1), was set in an sp^3 hybridization.[19] This pushes the $C_{1'}$ methyl group upward and allows the adjacent isoalloxazine ring to closely approach, forming a smooth cylindrical ribbon in agreement with higher-level DFT calculations.[19,28]

With previous work suggesting that 7/1 and 8/1 helices form around (6,5) and (8,6)-SWNTs, respectively, the question arises about what kind of helices prevail for intermediate NT diameters (i.e., 0.8−0.9 nm). For this, we examined two scenarios: (a) *helix dilation or contraction* to fit either larger or smaller nanotubes and (b) *fractional helices* capable of accommodating NTs with any d_t without dilation or contraction (Figure 1e).

Helix Dilation and Contraction. As shown by the solid red circles in Figure 5, the 7/1 FMN helix can be dilated up to 10% to fit a larger-d_t NT (indicated by the black arrow) before the individual lumiflavin moieties fly away. Such dilation mostly affects the lateral FMN−FMN interactions by weakening the H-bonding and vdW interactions that keep the helix together. The FMN 8/1 helix can tolerate a 5% contraction and at least a 7% dilation before the helix disassembles [black arrows on either side of the (8,6)-SWNTs]. Helix contraction, however, is more energetically expensive than dilation [i.e., larger energy departure for (9,4)- as opposed to (9,5)- and (8,7)-SWNTs]. Since the d_t difference between (6,5)- and (8,6)-SWNTs is 27%, dilation or contraction is incapable of bridging the d_t span, suggesting that fractional helices might be involved to wrap around intermediate-sized nanotubes [i.e., (8,4)- and (7,6)-SWNTs].
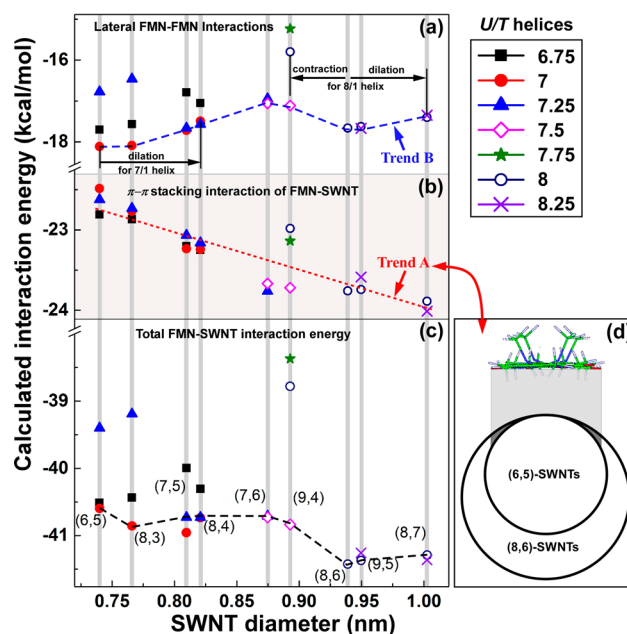
Figure 5. OPLSAA-calculated interaction energies for (a) FMN−FMN lateral packing, (b) FMN−nanotube $\pi-\pi$ stacking, and (c) total energy per one FMN moiety in various U/T helices wrapped around different (n,m)-SWNTs. (d) Cross-sectional view of the FMN interactions with (6,5)- and (8,6)-SWNTs. The dark-gray area schematically illustrates the reduction in $\pi-\pi$ stacking interactions due to higher nanotube curvature.

Fractional FMN Helices. Unlike 7/1 or 8/1 FMN helices, which employ seven or eight FMN dimers to complete one turn, fractional U/T FMN helices can be realized via translating the FMN dimer by $(2.5 \text{ nm} \times T)/U$ along the z axis while rotating by $(360° \times T)/U$ around the z axis using a radius of $d_t/2$ [of the given (n,m)-SWNT] + 0.34 nm (the helix−SWNT $\pi-\pi$ distance).[9b] In this fashion, a nanotube with any given d_t can be wrapped with the desired U/T FMN helix, defined by the net U/T ratio, which is either an integer or decimal number. With the understanding that (6,5)- and (8,6)-SWNTs naturally prefer 7/1 and 8/1 helices, four fractional helices bracketing the expected U/T ratio were constructed for each (n,m)-SWNT. For example, for (6,5)-SWNTs the following four U/T fractional helices were considered: $27/4 = 6.75$, $28/4 = 7$, $29/4 = 7.25$, and $30/4 = 7.5$. Following energy minimization, only the U/T fractional helices that produced stable assemblies around the given nanotube were further considered. Figure 5a−c and Table S2 report the calculated energies of the stable helices in terms of lateral FMN−FMN interactions (a), vdW contributions from $\pi-\pi$ stacking (b), and the total FMN−SWNT interaction energies (c). In total, seven fractional FMN helices with U/T ratios from 6.75 to 8.25 were found to make stable assemblies around SWNTs with $d_t = 0.76-1.03$ nm.

The relative magnitudes of the ordinates of Figure 5a,b versus Figure 5c, along with the mean values in Table S2, indicate that the $\pi-\pi$ stacking interactions are dominant (ca. 57.5%) in the overall helix stability as opposed to the weaker FMN−FMN lateral packing (ca. 42.5%). The good linear fit in all points of Figure 5b shows a progressive reduction in $\pi-\pi$ stacking interactions of FMN with NTs of higher curvatures (i.e., lower d_t). This is in agreement with the results of Ogunro and Wang,[28] as schematically illustrated in Figure 5d. The increasing π-orbital overlap between the flat isoalloxazine rings
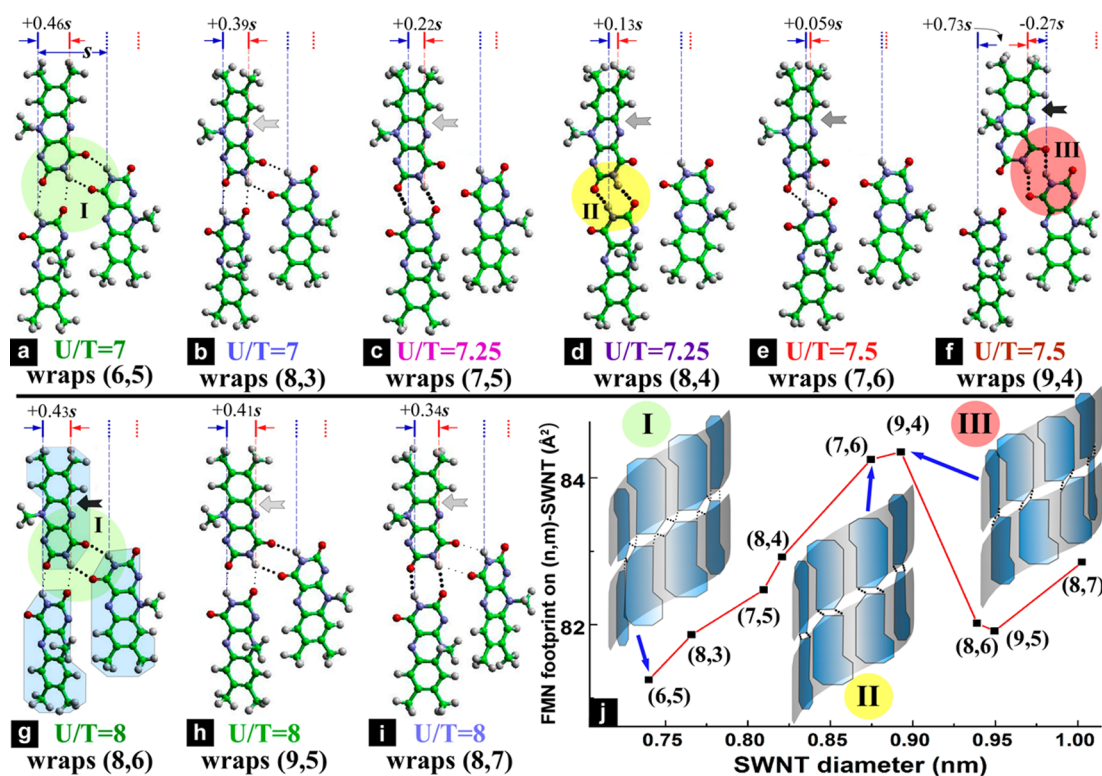
Figure 6. (a–i) Lumiflavin lateral packing in the optimum U/T helices around different (n,m)-SWNTs. As the U/T ratio progressively increases to host larger-d_t SWNTs, the top FMN moiety slides leftward (see the text for details). This results in the formation of three distinct types of H-bonds, shown as I, II, and III. The dependence of the average lumiflavin footprint in the aforementioned U/T helices (a–i) on the SWNT diameter is shown in (j). The insets in (j) illustrate the transitions between the three types of H-bonds as a function of nanotube diameter.

and the less-curved graphene sidewalls for larger SWNTs (trend A) provide an important insight for understanding the thermodynamic stability of these assemblies.

The next pattern that needs to be deciphered is the interpolated minima of the FMN–FMN lateral packing (trend B in Figure 5a). In doing so, it is important to review the three key factors that lead to the formation of the highly stable 8/1 helix around (8,6)-SWNTs (Figure 1d):

(i) The two sets of H-bonds (depicted by α and β) that link the adjacent isoalloxazine moieties into a two-dimensional (2D) ribbonlike pattern.[9a] This ribbon spirals around the nanotube with angle λ. The individual FMN units are mostly parallel with respect to the z axis (which also comprises the axes of the NT and FMN helices), albeit a small twist ($2 < \phi < 5°$) is oftentimes observed in the minimized structures. Figure 6g draws attention to the H-bonding pattern labeled as type I. This situates the top FMN unit roughly at the center (i.e., 43%) of the bottom two FMNs units, separated by a distance s. H-bond α (2.59 Å) is slightly longer than β (2.35 Å), and the two H-bonds have comparable N–H···O angles ($\delta = 140°$ and $\omega = 148°$, respectively) (Table S3). Table S4 depicts the H-bonding strengths for all of the energy-minimized U/T helices around various (n,m)-SWNTs. With 1.71 and 3.07 kcal/mol for the α and β H-bonds, respectively, the type-I helical FMN pattern around (8,6)-SWNTs constitutes the most stable configuration in terms of total H-bond strength (Table S4) and overall energy (Figure 5c).

(ii) The close molecular interdigitation among neighboring FMN units. As shown in Figure 1d, the two most prominent close contacts (2.4–2.6 Å) originate from the hydrogen atom at the C_6 position and a hydrogen atom of the methyl group at the

C_7 position.[9b] In order to optimize the neighboring lumiflavin organization, a knob-into-hole configuration is adopted, where the aforementioned two hydrogens (the knobs) are situated within the N_1–C_{10a}–N_{10} and N_{10}–C_{9a}–C_9–H crevices (the holes), respectively.

(iii) The sp^3 configuration of nitrogen atom N_{10}. This pushes the methyl substituent above the plane of the aromatic ring and renders nonrelevant the close contacts from the hydrogen atoms at the C_6 position and on the C_7 methyl group.[19]

On the basis of these three factors, the footprint of the lumiflavin can be expressed by the simplified "bootlike" blue tile depicted in Figure 1. With this at hand, the first test is to assess whether the OPLSAA-derived geometries are consistent with the earlier prediction that (6,5)-SWNTs are wrapped by a 7/1 FMN helix, which closely resembles that of the 8/1 for (8,6)-SWNTs.[9b] Figure S12a–c illustrates the assembly architectures of the three FMN helices ($U/T = 6.75$, 7, and 7.25) that form stable assemblies around (6,5)-SWNTs. The 6.75 fractional helix exhibits a radially compressed configuration that lowers β to 2.31 Å while expanding α to 2.85 Å. The slightly larger 7/1 helix brings α (2.64 Å) and β (2.40 Å) back within 98% of the distances witnessed in the type-I H-bond geometry. The larger 7.25 fractional helix radially dilates the assembly, which raises β to 2.41 Å while shortening α to 2.58 Å. These results verify our earliest prediction[9b] and explain why the 7/1 helix exhibits a greater FMN–FMN lateral interaction energy (Figure 5a). Correspondingly, the 7/1 helix around (6,5)-SWNTs closely resembles the type-I geometry of 8/1 around (8,6)-SWNTs. This geometry is shown as inset **I** in Figure 6j. Such packing combines both two sets of H-bonds and close molecular
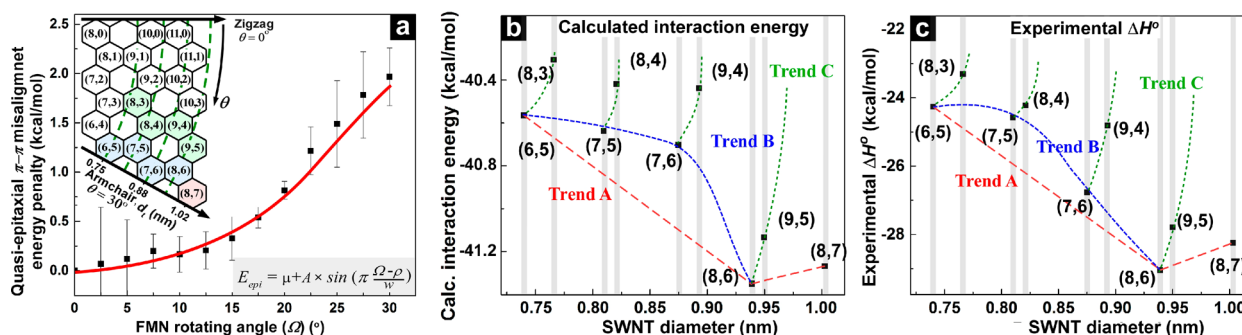
Figure 7. (a) Quasi-epitaxial $\pi-\pi$ misalignment energy penalty of lumiflavin on a graphene subunit as a function of twist angle (Ω). (b) OPLSAA-calculated interaction energy modified with the epitaxial misalignment energy penalty using the sinusoidal function in (a). The trend in (b) shows good resemblance to the experimentally determined $\Delta H°$ results of Figure 4b (H_2O medium), shown in (c). The sinusoidal fit in (a) was based on $\Omega = 30° - \theta - \phi$, where θ is the chiral angle for the different (n,m)-SWNTs shown in the Weisman plot inset and ϕ is the tilt angle of lumiflavin around various U/T helices (Figure S13). The parameter values are $\mu = 5767.52$, $A = 5767.59$, $\rho = 1782.91$, and $w = 3565.82$.

interdigitation of adjacent FMN tiles, visualized as a toe-to-heel stacking of the bootlike FMN tile in **I**.

The idealized 7/1 and 8/1 packing is not feasible for intermediate-diameter nanotubes. In order to increase the helix diameter (d_h), one needs to slightly "untwist" it. If the bottom half-ribbon of the FMN is fixed, untwisting requires the top half-ribbon to move from right to left, as shown by the solid arrows in Figure 6b−i. Such a slide displaces the top FMN unit from its center position ($0.46s$) for 7/1 to progressively lower values [i.e., $0.39s$, $0.22s$, $0.13s$, $0.06s$, and $-0.27s$ for (8,3), (7,5), (8,4), (7,6), and (9,4)-SWNTs, respectively], before returning it to the central position ($0.43s$) for the 8/1 helix, and this cycle is repeated for higher-d_t NTs. This stems from the additional fractional FMN unit that is added in the helix, raising its U/T value from 7 to 7.25 and 7.5, before it jumps back to 8 by skipping 7.75. This peculiar behavior finds its origins in the close molecular interdigitation between adjacent FMN units. Such interdigitation is apparent in all of the studied helices (Figure S12a−v). This indicates the premier importance of FMN interdigitation to the stability of FMN assemblies around various (n,m)-SWNTs. On the other hand, the familiar type-I H-bonding pattern is disrupted to yield different H-bonding arrangements. As the top FMN slides leftward, the originally strong β H-bond of the type-I pattern fades away and the weak α H-bond becomes stronger (Figure 6 and Table S4). This generates two new H-bonding configurations that are labeled as type II and type III (Figure 6d,f). Here it is important to stress that while types II and III forego the 2D H-bonding pattern of type I, the FMN ribbon retains its stability through its close molecular interdigitation with adjacent FMN units. The disruption of the second set of H-bonds, along with tight FMN−FMN interdigitation, is also expected to affect the helical packing density. The latter can be expressed in terms of an average FMN footprint, which progressively increases as the fractional helices around the indicated NTs become larger (i.e., from 7 to 7.25 and eventually 7.5) (Figure 6j). The largest FMN footprint (lowest helical density) is observed for (7,6) and (9,4), where type-II and -III H-bonding patterns are observed for both 7.5 helices. Additional untwisting of the helix (i.e., U/T = 7.75) becomes unstable, resulting in the sharp drop in FMN footprint to the slightly larger but highly stable 8/1 helix [i.e., (8,6)-, (9,5)-, and (8,7)-SWNTs]. What is noteworthy, however, is that the shape of the FMN footprint as a function of d_t bears a close resemblance to trend B in Figure 5a. This indicates that the lateral FMN−FMN packing stability is

directly governed by how close the lumiflavins approach each other within the given helical organization.

Now that both trend A in Figure 5b and trend B in Figure 5a have been addressed, the OPLSAA-calculated total interaction energy (black dashed line in Figure 5c) can be assessed. A quick comparison of Figures 5c and 4b shows that the total interaction energies are in only qualitative agreement with the experimentally determined $\Delta H°$ values for the near-armchair nanotubes and fail to address the chirality dependence [i.e., with the (8,3)-, (8,4)-, (9,4)-, and (9,5)-SWNTs having lower chiral angles ($\theta \approx 15-20°$)]. This arises from the inability of the OPLSAA force field to incorporate orbital-based $\pi-\pi$ interactions that are crucial for quasi-epitaxial isoalloxazine organization on top of the cylindrical graphene lattice. This will be addressed in the next section. Despite the lack of quasi-epitaxial consideration, OPLSAA-based MM provides a good reproduction of the energy envelope that governs FMN binding around near-armchair nanotubes. On this basis, it is valid to inquire about the relative strengths of $\pi-\pi$ stacking and lateral FMN−FMN interactions within the total system stability. Table S5 illustrates that $\pi-\pi$ stacking amounts to 55−58% of the total energy, with the remaining 45−42% resulting from lateral FMN−FMN interactions. It is also interesting to further separate the H-bonding contributions within the 45−42% lateral FMN−FMN contribution. For this, we used the atomic coordinates of the optimum U/T helices (Table S3) to calculate the H-bond strengths using the Dreiding force field (eq S1 in the SI and Table S4). On the assumption that OPLSAA and Dreiding energy calculations are comparable, the lateral FMN−FMN contribution is roughly split 3:1 between van der Waals + electrostatic FMN interdigitation and H-bonding interactions, respectively (Table S5).

Ab Initio Calculations. In order to accurately assess the energy penalty due to misalignment between the isoalloxazine rings and the given nanotube lattice, we turned our attention to dispersion-corrected DFT calculations. The large number of atoms involved with FMN/SWNT assemblies presents a major obstacle for such ab initio calculations. In an attempt to simplify the system, we decided to compute the $\pi-\pi$ stacking interactions of one lumiflavin molecule with a smaller (5 × 6) flat graphene subunit terminated with H atoms. For this, dispersion-corrected DFT[25] with the wb97xd/6-31G(d,p) basis set was employed.[26] At first, the lumiflavin was placed on the center of the graphene subunit and allowed to minimize its energy. Inset (a) of Figure S13 illustrates the optimized
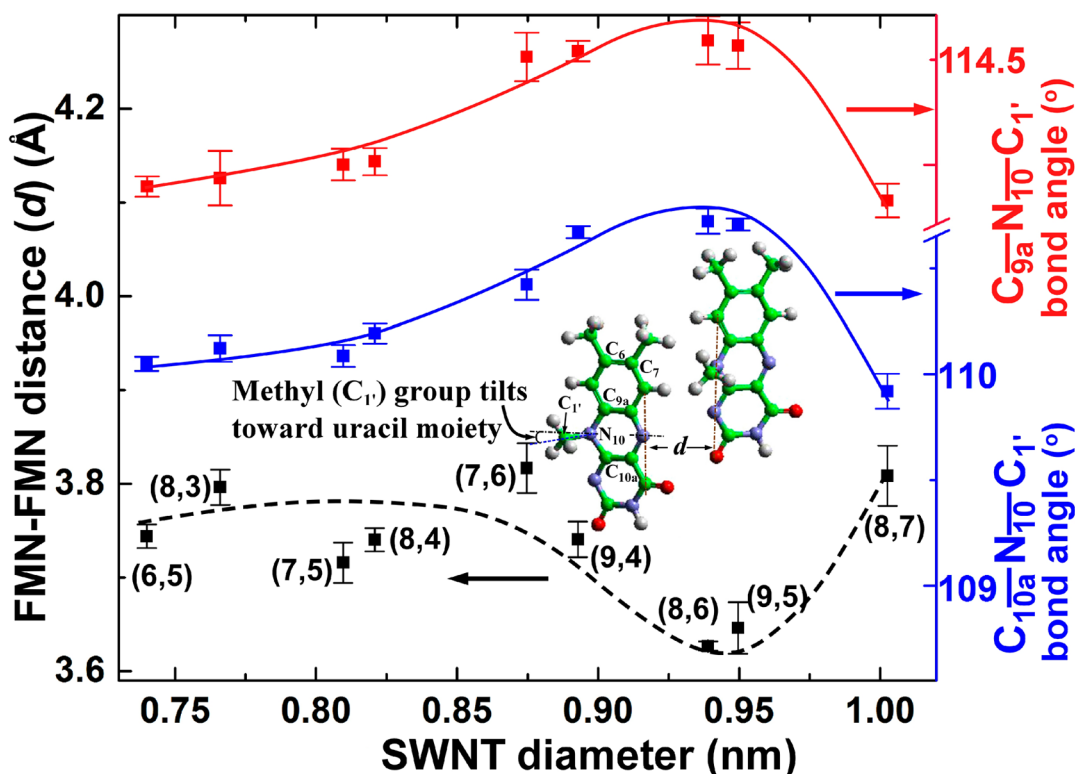
Figure 8. Bond angles of the sp^3 N$_{10}$ lumiflavin nitrogen and the FMN−FMN distance as functions of nanotube diameter. Solid and dashed curves are to guide the eye.

configuration, which bears a close resemblance to the "Bernal-type" orientation with a tilt angle $\Omega = 0°$. Subsequently, the lumiflavin was gradually rotated around its center of mass with a Ω interval of 2.5° until $\Omega = 30°$. The energy profile of such a rotation is shown in Figure S13 with blue circles, while insets (b) and (c) show the respective configurations for $\Omega = 15$ and 30°. In order to take into account the energy contribution of lumiflavins displaced away from the optimal Bernal stacking, the rotation profile of the most probable energy maximum [i.e., the bridge configuration,[34] where the center of mass between the N$_5$ and N$_{10}$ atoms of the lumiflavin is placed over the center of a graphene C−C bond; inset (d) in Figure S13] was also investigated. As rotation progresses, the bridge configuration goes through a local minimum with a near-Bernal orientation for two of the three rings [$\Omega = 15°$; inset (e)] before its energy increases for $\Omega = 30°$ [inset (f)]. Despite the different rotation energy trends of the two starting configurations, the average energy shown in Figure 7a produces a sinusoidal profile that closely resembles the behavior of similar systems of lesser complexity.[35] In light of the enormous dispersion in $\pi-\pi$ interactions between the various FMN entities comprising the helix and the curved graphene lattice, the sinusoidal function of Figure 7a provides a good estimate of quasi-epitaxial misalignment.[35]

Correspondingly, the MM-minimized structures of Figure 6 can be augmented with quasi-epitaxial misalignment penalty via setting $\Omega = 30° - \theta - \phi$. Table S6 lists the starting MM energy values and the added misalignment energy penalty based on the equation inset in Figure 7a. The combined MM + quasi-epitaxial interaction energies between lumiflavin and various (n,m)-SWNT lattices are shown in Figure 7b and contrasted with the experimentally determined $\Delta H°$ results (Figure 7c).[36] The incorporation of the quasi-epitaxial energy term affords a

satisfactory reproduction of trend C, which was missing from the MM calculations of Figure 5c. As shown with the color-coded Weisman plot inset in Figure 7a, trend C originates from the lower chiral angle of the (8,3)-, (8,4)-, (9,4)-, and (9,5)-SWNTs in relation to the near-armchair (6,5)-, (7,5)-, (7,6)-, and (8,6)-SWNTs possessing a better alignment with the FMN helix, which adopts the near-armchair configuration. The qualitative assessment of $\pi-\pi$ interactions in terms of the sum of vdW interactions (provided by OPLSAA) and orbital interactions (estimated by DFT), while crude, provides an accurate reproduction of the experimental results. This provides a simple yet powerful means to study multiatom assemblies that also involve quasi-epitaxial commensuration.

The last question that needs to be addressed is the upward inflection of trend A for (8,7)-SWNTs (Figure 7b,c). As shown in Figure 5, this ascent has its origins in the lateral FMN−FMN packing for (8,7)-SWNTs (Figure 5a), which far outweighs the greater $\pi-\pi$ stacking interactions from the reduced nanotube curvature (Figure 5b). The bottom (black) curve in Figure 8 presents the FMN−FMN distance (d) as a function of nanotube diameter, with the closest distances attained for (8,6)- and (9,5)-SWNTs. As the nanotube curvature decreases, close contacts between C$_{1'}$-methyl protons and adjacent C$_6$ and C$_7$-methyl protons are expected to make greater contributions to FMN−FMN repulsion (Figure 1). To assess this repulsion, the bond angles of the lumiflavin N$_{10}$ are coplotted as the upper two curves in Figure 8 and listed in Table S7. As the N$_{10}$ hybridization was set to sp^3, the magnitude of the departure from the 109.5° value is proportional to the stress exerted from such close contacts. With the C$_{9a}$−N$_{10}$−C$_{1'}$ bond angle consistently higher (by 4°) with respect to C$_{10a}$−N$_{10}$−C$_{1'}$ angle, it is apparent that the C$_7$ methyl group exerts greater repulsion (than the C$_6$ proton) of the C$_{1'}$ methyl group, which

tilts it toward the uracil moiety (Figure 8 inset). The nearly inverse correlation between the solid and dashed curves indicates the competition among vdW FMN interdigitation (manifested by lower d) and close-contact repulsions (from bending the $C_{1'}$ methyl group upward, which increases both N_{10} bond angles). As the nanotube curvature decreases and moves away from the optimum (8,6)- and (9,5)-SWNT FMN helices,[9a] a sharp deviation is witnessed for both d and the N_{10} bond angles for (8,7)-SWNTs. This explains why FMN does not effectively disperse SWNTs with d_t larger than (8,7) in H_2O. By increasing the hydrophobic interactions in D_2O, two additional SWNTs with larger d_t can be dispersed [i.e., (10,5) and (9,7)] before the aforementioned repulsion disrupts these helices as well (Figure 4b−d).

CONCLUSION

We have shown herein that the temperature-induced dissociation of FMN from its helical assembly provides an ideal system to extract high-fidelity thermodynamic stability values that govern nanotube−surfactant interactions. This reversible helix dissociation at higher temperatures exposes progressively larger portions of bare nanotube surfaces, which are prone to H^+/O_2 doping and photoluminescence quenching of the given nanotube. This eliminates possible interferences from the use of a second surfactant[9b,10,11] and provides thermodynamic stability values that can be readily modeled using molecular mechanics in combination with ab initio calculations. Our results indicate that the quasi-epitaxial interactions between the FMN isoalloxazine rings and the underlying graphene lattice constitute the majority of the enthalpic stabilization of the helix around various-chirality SWNTs. Close-packing interactions between adjacent isoalloxazine rings comprise the remaining stabilization contribution, which can be roughly split 3:1 between isoalloxazine electrostatic plus vdW interdigitation and H-bonding, respectively. The proportionally small H-bond contribution allows the formation of fractional helices with only one set of H-bonds (as opposed to two sets of H-bonds for the 7/1 and 8/1 helices) in order to wrap intermediate-diameter (d_t) nanotubes [between (6,5) and (8,6), respectively]. The helical stability rapidly decreases for SWNTs with $d_t > 1.0$ nm, stemming from the repulsion between the D-ribityl's $C_{1'}$ methyl group and the adjacent isoalloxazine ring due to reduced NT curvature. This study provides a comprehensive experimental and molecular modeling framework in order to study the complex surfactant−nanotube interactions around various-chirality nanotubes. Moreover, it improves our molecular understanding of the role that various FMN submoieties impart to the overall supramolecular stabilization and opens the door to the design of new systems with enhanced stability and functionality.

ASSOCIATED CONTENT

Ⓢ Supporting Information

Methods, UV−vis−NIR and PL spectra, and molecular mechanics and ab initio analyses. This material is available free of charge via the Internet at http://pubs.acs.org.

AUTHOR INFORMATION

Corresponding Author

papadim@mail.ims.uconn.edu

Notes

The authors declare no competing financial interest.

ACKNOWLEDGMENTS

REFERENCES

(1) (a) Dresselhaus, S.; Dresselhaus, G.; Avouris, P. *Carbon Nanotubes: Synthesis, Structure, Properties, and Applications*; Springer: Berlin, 2001. (b) Thess, A.; Lee, R.; Nikolaev, P.; Dai, H.; Petit, P.; Robert, J.; Xu, C.; Lee, Y. H.; Kim, S. G.; Rinzler, A. G.; Colbert, D. T.; Scuseria, G. E.; Tománek, D.; Fischer, J. E.; Smalley, R. E. *Science* **1996**, *273*, 483.

(2) (a) Bonaccorso, F.; Hasan, T.; Tan, P. H.; Sciascia, C.; Privitera, G.; Di Marco, G.; Gucciardi, P. G.; Ferrari, A. C. *J. Phys. Chem. C* **2010**, *114*, 17267. (b) Islam, M. F.; Rojas, E.; Bergey, D. M.; Johnson, A. T.; Yodh, A. G. *Nano Lett.* **2003**, *3*, 269. (c) O'Connell, M. J.; Bachilo, S. M.; Huffman, C. B.; Moore, V. C.; Strano, M. S.; Haroz, E. H.; Rialon, K. L.; Boul, P. J.; Noon, W. H.; Kittrell, C.; Ma, J.; Hauge, R. H.; Weisman, R. B.; Smalley, R. E. *Science* **2002**, *297*, 593.

(3) (a) Vaisman, L.; Wagner, H. D.; Marom, G. *Adv. Colloid Interface Sci.* **2006**, *128−130*, 37. (b) Lin, Y.; Taylor, S.; Li, H.; Fernando, K. A. S.; Qu, L.; Wang, W.; Gu, L.; Zhou, B.; Sun, Y.-P. *J. Mater. Chem.* **2004**, *14*, 527. (c) Chen, R. J.; Zhang, Y.; Wang, D.; Dai, H. *J. Am. Chem. Soc.* **2001**, *123*, 3838.

(4) Moore, V. C.; Strano, M. S.; Haroz, E. H.; Hauge, R. H.; Smalley, R. E.; Schmidt, J.; Talmon, Y. *Nano Lett.* **2003**, *3*, 1379.

(5) (a) Haggenmueller, R.; Rahatekar, S. S.; Fagan, J. A.; Chun, J.; Becker, M. L.; Naik, R. R.; Krauss, T.; Carlson, L.; Kadla, J. F.; Trulove, P. C.; Fox, D. F.; DeLong, H. C.; Fang, Z.; Kelley, S. O.; Gilman, J. W. *Langmuir* **2008**, *24*, 5070. (b) Lin, S.; Blankschtein, D. *J. Phys. Chem. B* **2010**, *114*, 15616. (c) Samarajeewa, D. R.; Dieckmann, G. R.; Nielsen, S. O.; Musselman, I. H. *Nanoscale* **2012**, *4*, 4544. (d) Debnath, S.; Cheng, Q.; Hedderman, T. G.; Byrne, H. J. *J. Phys. Chem. C* **2010**, *114*, 8167. (e) Gotovac, S.; Honda, H.; Hattori, Y.; Takahashi, K.; Kanoh, H.; Kaneko, K. *Nano Lett.* **2007**, *7*, 583. (f) Hedderman, T. G.; Keogh, S. M.; Chambers, G.; Byrne, H. J. *J. Phys. Chem. B* **2006**, *110*, 3895.

(6) Tu, X.; Manohar, S.; Jagota, A.; Zheng, M. *Nature* **2009**, *460*, 250.

(7) Star, A.; Steuerman, D. W.; Heath, J. R.; Stoddart, J. F. *Angew. Chem., Int. Ed.* **2002**, *41*, 2508.

(8) (a) Nish, A.; Hwang, J.-Y.; Doig, J.; Nicholas, R. J. *Nat. Nanotechnol.* **2007**, *2*, 640. (b) Kang, Y. K.; Lee, O.-S.; Deria, P.; Kim, S. H.; Park, T.-H.; Bonnell, D. A.; Saven, J. G.; Therien, M. J. *Nano Lett.* **2009**, *9*, 1414. (c) Liu, J.; Moo-Young, J.; McInnis, M.; Pasquinelli, M. A.; Zhai, L. *Macromolecules* **2014**, *47*, 705. (d) Stranks, S. D.; Habisreutinger, S. N.; Dirks, B.; Nicholas, R. J. *Adv. Mater.* **2013**, *25*, 4365.

(9) (a) Ju, S.-Y.; Doll, J.; Sharma, I.; Papadimitrakopoulos, F. *Nat. Nanotechnol.* **2008**, *3*, 356. (b) Ju, S.-Y.; Kopcha, W. P.; Papadimitrakopoulos, F. *Science* **2009**, *323*, 1319.

(10) Kato, Y.; Inoue, A.; Niidome, Y.; Nakashima, N. *Sci. Rep.* **2012**, *2*, No. 733.

(11) Oh, H.; Sim, J.; Ju, S.-Y. *Langmuir* **2013**, *29*, 11154.

(12) Sharifi, R.; Abanulo, D. C.; Papadimitrakopoulos, F. *Langmuir* **2013**, *29*, 7209.

(13) (a) Petersheim, M.; Turner, D. H. *Biochemistry* **1983**, *22*, 256. (b) Borer, P. N.; Dengler, B.; Tinoco, I., Jr.; Uhlenbeck, O. C. *J. Mol. Biol.* **1974**, *86*, 843.

(14) (a) Lee, J. C.; Timasheff, S. N. *J. Biol. Chem.* **1981**, *256*, 7193. (b) Gekko, K.; Timasheff, S. N. *Biochemistry* **1981**, *20*, 4677. (c) Brandts, J. F. *J. Am. Chem. Soc.* **1964**, *86*, 4291.

(15) Stryer, L. *Biochemistry*, 4th ed.; Freeman: New York, 1995.

(16) Brenner, D. W.; Shenderova, O. A.; Harrison, J. A.; Stuart, S. J.; Ni, B.; Sinnott, S. B. *J. Phys.: Condens. Matter* **2002**, *14*, 783.

(17) Jorgensen, W. L.; Maxwell, D. S.; Tirado-Rives, J. *J. Am. Chem. Soc.* **1996**, *118*, 11225.

(18) Plimpton, S. *J. Comput. Phys.* **1995**, *117*, 1.

(19) Ju, S.-Y.; Abanulo, D. C.; Badalucco, C. A.; Gascón, J. A.; Papadimitrakopoulos, F. *J. Am. Chem. Soc.* **2012**, *134*, 13196.

(20) Bayly, C. I.; Cieplak, P.; Cornell, W.; Kollman, P. A. *J. Phys. Chem.* **1993**, *97*, 10269.

(21) Yang, Z.; Wang, Z.; Tian, X.; Xiu, P.; Zhou, R. *J. Chem. Phys.* **2012**, *136*, No. 025103.

(22) Frey, J. T.; Doren, D. J. *TubeGen*; University of Delaware: Newark, DE, 2010; http://turin.nss.udel.edu/research/tubegenonline.html.

(23) (a) Sherrill, C. D.; Sumpter, B. G.; Sinnokrot, M. O.; Marshall, M. S.; Hohenstein, E. G.; Walker, R. C.; Gould, I. R. *J. Comput. Chem.* **2009**, *30*, 2187. (b) Balamurugan, K.; Gopalakrishnan, R.; Raman, S. S.; Subramanian, V. *J. Phys. Chem. B* **2010**, *114*, 14048. (c) Paton, R. S.; Goodman, J. M. *J. Chem. Inf. Model.* **2009**, *49*, 944.

(24) Lazar, P.; Karlický, F.; Jurečka, P.; Kocman, M.; Otyepková, E.; Šafářová, K.; Otyepka, M. *J. Am. Chem. Soc.* **2013**, *135*, 6372.

(25) Chai, J.-D.; Head-Gordon, M. *Phys. Chem. Chem. Phys.* **2008**, *10*, 6615.

(26) Frisch, M. J.; Trucks, G. W.; Schlegel, H. B.; Scuseria, G. E.; Robb, M. A.; Cheeseman, J. R.; Scalmani, G.; Barone, V.; Mennucci, B.; Petersson, G. A.; Nakatsuji, H.; Caricato, M.; Li, X.; Hratchian, H. P.; Izmaylov, A. F.; Bloino, J.; Zheng, G.; Sonnenberg, J. L.; Hada, M.; Ehara, M.; Toyota, K.; Fukuda, R.; Hasegawa, J.; Ishida, M.; Nakajima, T.; Honda, Y.; Kitao, O.; Nakai, H.; Vreven, T.; Montgomery, J. A., Jr.; Peralta, J. E.; Ogliaro, F.; Bearpark, M.; Heyd, J. J.; Brothers, E.; Kudin, K. N.; Staroverov, V. N.; Kobayashi, R.; Normand, J.; Raghavachari, K.; Rendell, A.; Burant, J. C.; Iyengar, S. S.; Tomasi, J.; Cossi, M.; Rega, N.; Millam, J. M.; Klene, M.; Knox, J. E.; Cross, J. B.; Bakken, V.; Adamo, C.; Jaramillo, J.; Gomperts, R.; Stratmann, R. E.; Yazyev, O.; Austin, A. J.; Cammi, R.; Pomelli, C.; Ochterski, J. W.; Martin, R. L.; Morokuma, K.; Zakrzewski, V. G.; Voth, G. A.; Salvador, P.; Dannenberg, J. J.; Dapprich, S.; Daniels, A. D.; Farkas, Ö.; Foresman, J. B.; Ortiz, J. V.; Cioslowski, J.; Fox, D. J. *Gaussian 09*; Gaussian, Inc.: Wallingford, CT, 2009.

(27) Woods, L. M.; Bǎdescu, Ş. C.; Reinecke, T. L. *Phys. Rev. B* **2007**, *75*, No. 155415.

(28) Ogunro, O. O.; Wang, X.-Q. *Nano Lett.* **2009**, *9*, 1034.

(29) Kim, S. N.; Luo, Z.; Papadimitrakopoulos, F. *Nano Lett.* **2005**, *5*, 2500.

(30) Cognet, L.; Tsyboulski, D. A.; Rocha, J.-D. R.; Doyle, C. D.; Tour, J. M.; Weisman, R. B. *Science* **2007**, *316*, 1465.

(31) Miyauchi, Y.; Matsuda, K.; Yamamoto, Y.; Nakashima, N.; Kanemitsu, Y. *J. Phys. Chem. C* **2010**, *114*, 12905.

(32) Tabakman, S. M.; Welsher, K.; Hong, G.; Dai, H. *J. Phys. Chem. C* **2010**, *114*, 19569.

(33) (a) Ozawa, T.; Asakawa, T.; Garamus, V. M.; Otha, A.; Miyagishi, S. *J. Oleo Sci.* **2005**, *54*, 585. (b) Soper, A. K. *Phys. Rev. Lett.* **2008**, *101*, No. 065502. (c) Luan, C.-h.; Urry, D. W. *J. Phys. Chem.* **1991**, *95*, 7896.

(34) Ershova, O. V.; Lillestolen, T. C.; Bichoutskaia, E. *Phys. Chem. Chem. Phys.* **2010**, *12*, 6483.

(35) Feng, X.; Marcon, V.; Pisula, W.; Hansen, M. R.; Kirkpatrick, J.; Grozema, F.; Andrienko, D.; Kremer, K.; Müllen, K. *Nat. Mater.* **2009**, *8*, 421.

(36) Replotted from Figure 4b, black squares.